Optimisation of sample geometry for thermo-mechanical testing of precipitation hardenable nickel-based superalloys with an ETMT machine

M. King[1*], S. Rahimi[1]

[1]Advanced Forming Research Centre (AFRC), University of Strathclyde, 85 Inchinnan Drive, Inchinnan, Renfrew, PA4 9LJ.

Abstract

Accurate determination of thermo-mechanical properties in precipitation hardenable materials using an electro-thermal mechanical testing (ETMT) system is a well-established challenge. The non-uniform distribution of temperature resulting from heating based on the joule effect (i.e., resistivity heating), leads to heterogeneous deformation along the gauge length, owing to the temperature dependency of mechanical properties, which makes their direct measurements complicated. This study presents an evaluation of four different miniaturised sample geometries which were tested to achieve an optimised sample with acceptable uniform strain and temperature distributions in the gauge volume. In-situ displacement mapping, using digital image correlation (DIC), was utilised to calibrate the optimised sample dimensions with the aim of forcing the deformation to the hottest region of the gauge lengths during the tests. Tests were carried out on Inconel 718 (IN718) at 720˚C, an optimal temperature for the precipitation of γ", the primary strengthening particle in this alloy. The results showed that only in the case of the geometry proposed in this study (i.e., a sample with a short gauge length (~ 2 mm)) did the deformation acceptably localise at the centre, compared to other geometries. A correction methodology is developed which equates the strain measured using DIC over the 2mm gauge length of the modified sample geometry with the strain measured using the Linear Variable Differential Transformer (LVDT) integrated to the

*Corresponding author:

E-mail address: michael.king@strath.ac.uk

Tel: +44 (0) 141 534 5261

Fax: +44 (0) 141 562 3387

This is a peer reviewed, accepted author manuscript of the following research article: King, M., & Rahimi, S. (2023). Optimisation of sample geometry for thermo-mechanical testing of precipitation hardenable nickel-based superalloys with an ETMT machine. *Strain*. https://doi.org/10.1111/str.12458

ETMT, making future tests on IN718, and other precipitation hardenable materials, possible without the need for use of a DIC system.

Keywords: Electro-Thermal Mechanical Testing (ETMT), Nickel-based superalloy, Mechanical properties, Digital Image Correlation (DIC), Deformation and strain mapping, micro-mechanical testing

1 Introduction

Understanding materials thermo-mechanical properties is vital for the optimisation of manufacturing process parameters (e.g., during forging), and for the prediction of their behaviours in service. Determination of these properties can be difficult, time consuming and costly, especially at elevated temperatures and under high strain rates; this makes the introduction of new alloys, qualified for applications, extremely difficult [1, 2]. In particular the cost for the production of enough material for testing can be excessive, as can the facilities required for the determination of thermo-mechanical properties, often beyond justification. This becomes even more problematic when testing high value components such as those made from a single crystal (e.g., gas turbine aerofoils).

The mechanical properties of materials vary with temperature and as such, mechanical testing at elevated temperatures is often required to gain a clearer understanding of materials behaviour. Conventional testing rigs typically equipped with convection and/or induction furnaces for heating the test piece to the target temperature, are often used as the means for testing materials thermo-mechanical behaviours. The time taken for these furnaces to reach and stabilise at the test temperature vary depending on the target temperature, the size of the specimen, as well as the type of furnace used. This is usually no quicker than 20 minutes for testing medium scale samples [3]. Within this period, before the commencement of the mechanical test and whilst the sample is reaching the target temperature and stabilising, there are often microstructural changes taking place which affect the mechanical properties and are not captured in the test results. This is because the sample is in such a dynamic state whilst heating for a prolonged period of time. The inability of the conventional test rigs in capturing these microstructural changes which take place during heat-up, and the long heat-up time itself, are of course disadvantages. However, these are not the only challenges, for instance adhering to ASTM standards E8/E8M-21 [4] and E21-20 [5], which require fairly large sized samples used for tensile testing, can be disadvantageous for manufacturing samples from costly materials such as aerospace grades nickel-based superalloys and titanium alloys. Furthermore, if the sample is to be manufactured from a part, as is often the case, and the part is small or complicated, it can be impossible to cut out a full-sized specimen. Undoubtedly, such challenges lead to prolonged

experimental approaches using alternative methods to optimise forging conditions and to certify materials for service conditions.

To combat some of these challenges, the National Physical Laboratory (NPL), in conjunction with Instron, developed the ETMT system capable of performing tests to assess both the thermo-mechanical and the thermo-physical properties of materials [6]. One of the major advantages of the ETMT system is its swift heating that is based on a material's electrical resistivity. It maintains temperature control through the use of water-cooled grips at the top and bottom of a sample. Despite its advantages in heating up samples to the target temperature at very fast rates, as well as the capability of very fast cooling rates, the very physical nature of the assembly (i.e., cooling grips) leads to a parabolic distribution of temperature along the length of the sample with the hottest part being in the middle of the gauge length [7, 8]. This leads to two distinct challenges. Firstly, this non-uniform distribution of temperature leads to a heterogeneous deformation (i.e., strain) along the gauge length due to the dependency of materials mechanical properties on temperature and the development of an effective gauge length, which makes the direct measurement of these properties complicated. The effective gauge length is a shorter region within the gauge length of a sample where the peak of the parabolic temperature distribution normally causes all of the strain to localise [6]. This can be seen in Fig. 1a. Linear engineering strain (ε) is defined as,

Equation 1

$$\varepsilon = \frac{\Delta L}{L_0}$$

where ΔL is the change in length of a sample and L_0 is the initial gauge length, in this case meaning the effective gauge length. Fig. 1b shows three example stress-strain curves which all derive from the same data (meaning the crosshead displacement [ΔL] is the same in all tests) but with different effective gauge lengths selected. Selecting a smaller effective gauge length (L_0) than appropriate will have the effect of increasing the engineering strain which will subsequently make the material appear to have a lower stiffness and a greater elongation. Equally selecting an unduly large effective gauge length will have the opposite effect and critically can lead to the appearance of premature failure in the material. If the strain value is calculated over a gauge length of 6mm, but the effective gauge length is actually 2mm, then the localised strain magnitude at the effective gauge length is far higher than the calculated value meaning it will appear to fail sooner. It can therefore be seen that an accurate determination of the effective gauge length is crucial for determining the materials mechanical properties. The NPL good practice guide recommends determining this effective gauge length using finite element methods or by

experimentation. Both of these methods have significant challenges. A finite element approach requires a material model which may not be available, and performing several exploratory tests to determine the effective gauge length experimentally can be time consuming and costly, especially if the material being investigated itself is expensive, as is often the case for tests carried out with the ETMT.

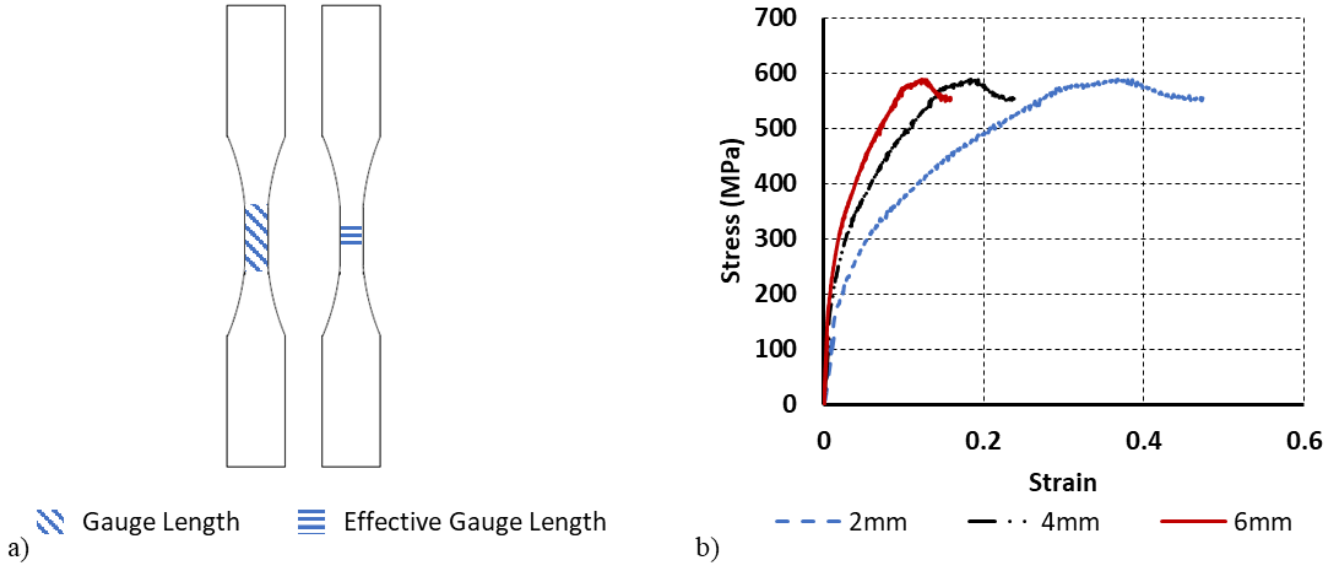

Fig. 1 a) Dog-bone sample showing the difference between the gauge length and the effective gauge length and b) example stress-strain curves showing the impact of 3 different effective gauge lengths of 2mm, 4mm, and 6mm.

The second distinct challenge created by the parabolic temperature distribution, relates to the class of material being tested. For most materials, the hottest region typically becomes the weakest and undergoes deformation under comparatively lower loads. This is however not the case for precipitation hardenable materials such as different grades of nickel-based superalloys for aerospace applications (e.g., turbine discs), where the hottest part of the specimen can become the strongest depending on temperature[3]. This can lead to a drift in plastic deformation away from the hot mid-gauge section of the sample, where the temperature is known, out towards the end of the gauge length where the temperature is significantly lower and unknown. It is possible to estimate the temperature at the outer gauge length by using numerical approaches, but this often leads to erroneous results [9]. In this instance, if the crosshead displacement is used as the basis for the evaluation of strain, then the determination of the materials mechanical properties, and the level of plastic deformation becomes compromised as the displacement is coming from regions at the edge of the gauge length where the temperature is unknown, and not in the middle of the gauge length where the temperature is recorded. This very phenomenon is mentioned in the NPL good practice guide [6], especially for precipitation hardened nickel-based superalloys over a temperature range (i.e., aging temperatures) where different strengthening particles are stable [3, 10, 11].

A recent study [12] has attempted to address this issue by using DIC to measure the displacement map, in-situ, from which the strain has then been evaluated. However, this study has only used a scaled-down sample geometry on a single crystal that may not be applicable to all nickel-based superalloys. In the present study, the existing sample geometry recommended by NPL's good practice guide [6], and also a number of other geometries, including both modified and adopted from previous reports[6, 12, 13], have been tested with an ETMT, in-situ, using DIC to track the spread of deformations, to find a geometry most suitable to satisfy three critical conditions. Firstly, the deformation (and hence strain) must be centred at the middle of the gauge length with no measurable drift. This will give confidence that the plastic strain and mechanical properties are for the recorded temperature and not an unknown, cooler temperature closer to the grips. Secondly, the size of the effective gauge length must be known, preferably prior to test commencement. This means there would be homogenous deformation across the effective gauge length allowing for a far easier determination of the materials plastic strain and mechanical properties. Thirdly and finally, the temperature distribution across the effective gauge length must be within 1% of the recorded temperature at the centre of the sample. ASTM E21-20 states that the temperature must not exceed ±3˚C for test temperatures of 1000˚C and ±6˚C for test temperatures above 1000˚C when heated with a convection furnace. The parabolic temperature distribution present in the case of the ETMT makes these limits very challenging, so a more achievable target of 1% of the recorded temperature at the centre of the sample was selected. Only when all three of these criteria are satisfied will a geometry be classed as suitable. These tests are conducted on IN718, a nickel-based superalloy, over a range of temperatures that are used in industry for forging process and subsequent aging heat treatments. A thermal imaging camera was used on the sample which satisfied the above criteria best, as well as on the rectangular geometry recommended in the NPL's good practice guide [5], to investigate the temperature distributions. Finally, a set of interrupted mechanical tests were carried out using the best performing sample geometry for the determination of mechanical properties to compare with existing data on IN718 in literature.

2 Experimental procedures

2.1 Material and samples

All test samples were manufactured from a 2000 mm × 250 mm diameter billet of IN718 nickel-based superalloy in the as-aged condition, supplied by Aubert & Duval (A&D). The nominal chemical composition for this material, supplied by the manufacturer, is provided in Table 1. Specimens were cut out using an electrical discharge

machine (EDM) and tested in the as-received condition. All samples were cut in the same direction to avoid any potential impact of mechanical anisotropy on the test results.

Table 1 - Nominal chemical composition of the IN718 material used in this study, provided by the manufacturer.

Element	Ni	C	Fe	Cr	Nb	Mo	Ti	Al
Wt.%	Bal.	0.04	18.50	18.00	5.20	3.00	0.90	0.50

Four different sample geometries were tested, including (i) rectangular sample, recommended by the NPL good practice guide for testing with the ETMT system [6]; (ii) standard tensile sample (hereby referred to as the dog-bone sample), which is a scaled-down classic dog-bone shape slightly modified from the NPL good practice for testing with the ETMT system for nickel-based superalloys [6]; (iii) winged sample, adopted from a methodology developed for thermo-mechanical testing with increased uniform temperature distribution using a Gleeble thermal-mechanical physical simulation system which is similar to the ETMT system in principal [13]; and (iv) modified dog-bone sample, developed during the course of this study and hereby referred to as the short gauge length sample. The optimisation criteria for development of the short gauge length sample was to force the deformation to the hottest area of the sample (i.e. centre of the gauge length). This was (i) to equate the gauge length and the effective gauge length to the same size, i.e., homogenous deformation across the gauge length for far easier determination of the materials plastic strain and mechanical properties, and (ii) to have a temperature distribution across the effective gauge length of no more than ±1% of the recorded temperature at the centre of the sample. There were three key design variables which were taken into consideration to meet the optimisation criteria. The gauge length of the sample was reduced from the 6mm of the winged sample and 5mm of the dog-bone sample, to 2mm to make the gauge length and effective gauge length the same size. Having sharper fillets of 1.5mm radius as opposed to 20mm radius in an attempt to prevent strain migration from the centre and the deformation encroaching on the cross-sectional area at the fillets which is unknown and larger than the cross-sectional area at the gauge length, hence it would impact the stress values and was undesirable. Finally the maximum width of the sample could be no more than 6mm in order to fit between the screws in the grips. A value of 5mm was selected to allow 1mm for clearance. Fig. 2 shows schematic sketches for these geometries with all the relevant dimensions provided.

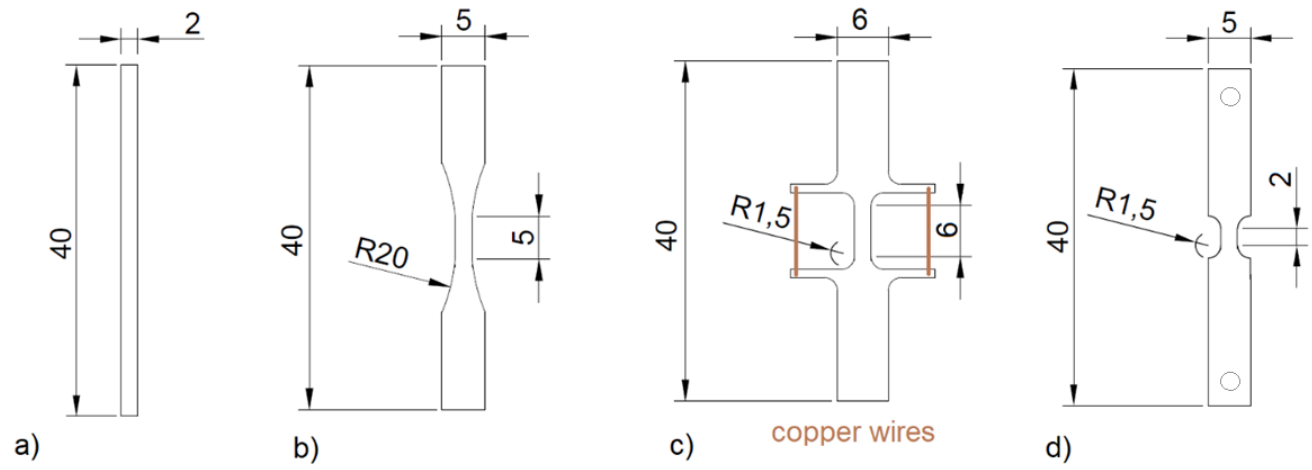

Fig. 2 – Four sample geometries investigated in this study for testing with the ETMT system, (a) rectangular, (b) dog-bone, (c) winged, and (d) short gauge length. All dimensions are in mm. Note: in (c) the coloured lines connecting the wings are schematic representation of the copper wires used to create an electric short-cut.

2.2 Thermo-Mechanical Testing

2.2.1 Equipment and methodology

The experiments were carried out using an Instron© ETMT 8800 system, equipped with a mechanical assembly capable of testing in tension and compression up to a maximum load of 5 kN. A customised gripping system was designed in-house, to accommodate samples of different geometries with a high accuracy and repeatable alignment. The grips were sand-blasted to increase the friction coefficient and reduce the potential for slip in the samples without pinholes. The sample gripping assembly was water cooled during operation for temperature control. The samples were heated with the aid of a 400 A DC power supply based on electrical resistivity (i.e., the Joule effect). For each test, the temperature was measured and controlled through an R-type thermo-couple, composed of 0.1 mm diameter wires consisting of platinum and platinum-13% rhodium, spot-welded to the sample at the centre of the gauge length under a condition where a bead was formed as a result of melting both wires. Fig. 3 shows the basic ETMT assembly and Fig. 4**Error! Reference source not found.** shows an image of a typical bead formed during spot-welding.

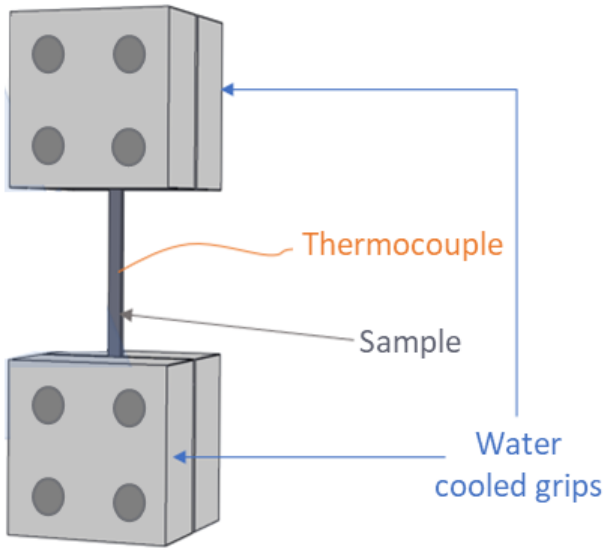

Fig. 3 Sketch of the experimental set-up demonstrating the basic ETMT grips and the area explored by DIC.

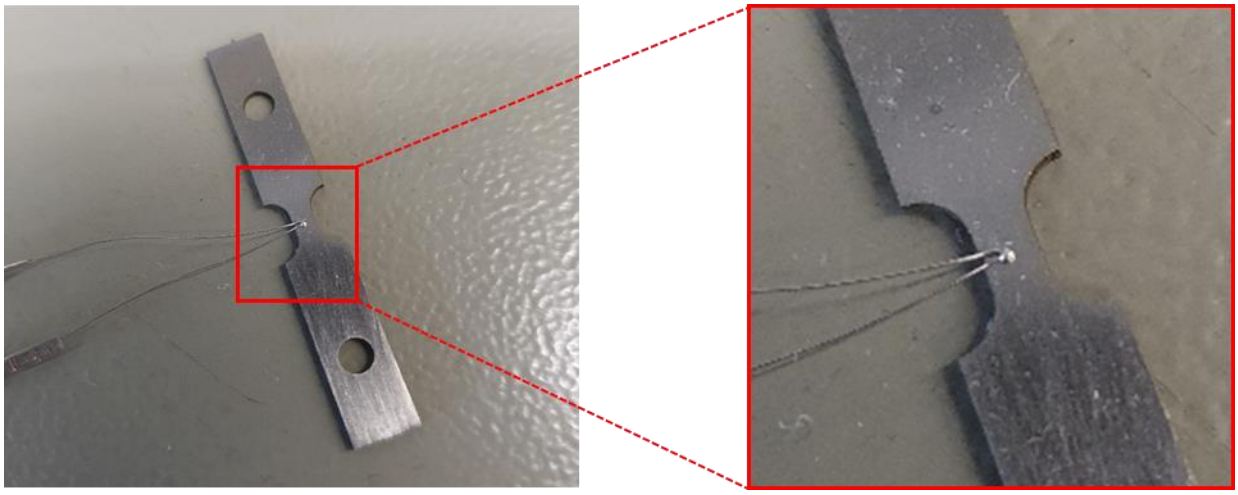

Fig. 4 Photograph of a short gauge length sample with a thermocouple bead spot-welded onto the middle of the gauge length.

During each mechanical test, displacement of the top moving grip was measured with a built-in Linear Variable Differential Transformer (LVDT). Concurrently, the surface strain along and across the gauge length for each sample was measured during the test using a 3D DIC system, which was capable of mapping in-plane and out of plane displacements. Ten images were captured at one second intervals, and the displacements in the x and y directions (denoted u and v, respectively) were measured. Consequently, the strain in the x, y, and xy directions (denoted ε_{xx}, ε_{yy}, and ε_{xy}, respectively) were calculated using the same settings as for the actual tests whilst at temperature. Both the spatial and temporal standard deviations (STD's) were computed to understand the level of uncertainty associated with the DIC measurements as can be seen in Table 2. The values for displacement and

strain are an order of magnitude higher than what has been reported in literature for noise values calculated at room temperature, but are in line with noise values calculated at elevated temperatures as was the case in these tests[14, 15].

Table 2 –Noise floor given by spatial and temporal standard deviations for each test.

	U (pixel)		V (pixel)		ε_{xx} (%)		ε_{yy} (%)		ε_{xy} (%)	
Sample Geometry	**Spatial STD**	**Temporal STD**	**Spatial STD**	**Temporal STD**	**Spatial STD**	**Temporal STD**	**Spatial STD**	**Temporal STD**	**Spatial STD**	**Temporal STD**
Rectangular	0.119	0.258	0.093	0.175	0.079	0.053	0.047	0.047	0.038	0.031
Winged	0.039	0.087	0.047	0.070	0.024	0.023	0.025	0.026	0.014	0.017
Dog-bone	0.048	0.139	0.042	0.084	0.018	0.030	0.022	0.031	0.013	0.020
Short-Gauge length	0.074	0.134	0.039	0.088	0.036	0.047	0.039	0.042	0.027	0.032

For the measurement of surface displacement with DIC, a fine speckle pattern was produced on the surface in the area of interest, using a white high temperature paint as a background with an overspray of a black paint of the same type. This method has been shown to produce a consistent pattern with high contrast between features at elevated temperatures which makes it ideal for this application [12, 16]. The resulting pattern with random distributions of fine objects with light, dark, and grey contrast offered an appropriate number of features for tracking. It is important to note that the speckle pattern deteriorated when held at temperature, though the contrast was good enough for tracking displacements by DIC. An example of a surface with speckle patterns at room and elevated temperatures are provided in Fig. 5. As the spatial and temporal standard deviations were calculated at elevated temperatures when the speckle pattern had deteriorated, the impact of texture evolution of the paint has been mitigated as much as possible.

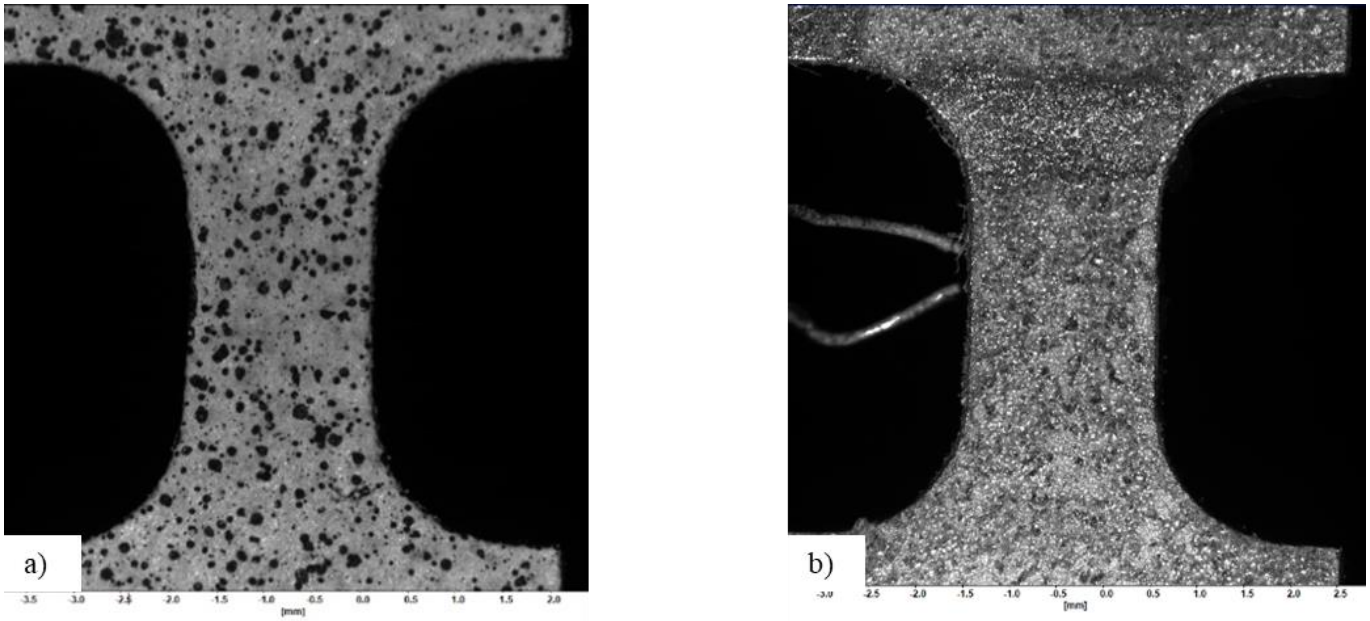

Fig. 5 Examples of surfaces with speckle patterns (a) at room temperature, and (b) at 770˚C, prepared for displacement mapping during thermo-mechanical testing with the ETMT system.

Consecutive images of the sample surface were recorded using LaVision's MX4M digital cameras installed on a Zeiss Discovery V12 3D stereo microscope. To eliminate any possible black body radiation emitting from the sample whilst at temperature, blue LED lights and a filter were used during image acquisition. For each test, images were recorded from the beginning of the test to the end at a frequency of 10 Hz using an incremental correlation mode, meaning each image is correlated to the previous image and each incremental deformation is summed. This increases the amount of error in the correlation compared to a correlation with a single reference image, however for large displacements where the DIC pattern is likely to change substantially, this is the preferred method. Analogue signals for load, LVDT, and temperature transmitted from the ETMT, were connected to the DIC system through a signal interface unit. This enabled the relevant data to be collected and recorded in real-time and used for synchronising the mechanical test data measured by the ETMT with those of the DIC. The images obtained during the tests were analysed by the LAVision DaVis image correlation software (version 8.3.0) to evaluate the strain maps. The International Digital Image Correlation Society's good practice guide recommends a practical subset size of 21 × 21 pixel^2 for correlation [17], however as these tests had features which were larger and more sparse, the strain maps were obtained using a 41 × 41 pixel^2 subset size. The same good practice guide recommends that the step size is between one-third to one-half of the subset size [17], so a step size of 20 was selected. A second order polynomial smoothing filter with 3 × 3 pixel^2 was used to smooth the results and reduce noise. Comparison with unfiltered results showed no significant bias. In these tests one pixel

was equivalent to 5.2 μm, except for the case of the short gauge length sample, where field of view was less of a priority so the magnification was increased slightly so that one pixel was 3.65μm. The Fast-Fourier transform algorithm was used to correlate the images.

2.2.2 Effect of sample geometry on deformation

For the evaluation of a suitable sample geometry, the thermo-mechanical test procedure started with heating the sample to 980°C at a 10 °C/s heating rate, dwelled at this temperature for ten minutes to annihilate any pre-existing residual stress and to dissolve the γ' and γ'' precipitates present. This heat treatment resembles the final closed die forging operation which is typically done at 980 °C for IN718, and normalises the microstructure of all samples relative to one another in the gauge length. The sample was then cooled at a rate of 50 °C/s (i.e., to resemble the quenching condition) to the target test temperature at 720°C and soaked for 2 minutes to allow the temperature to homogenise throughout the gauge length. The aging temperature of 720°C is an optimised temperature for effective precipitation of γ'' and hence was selected for these analyses. The rationale was to understand the effect of the onset of precipitation at aging temperatures on the evolution of residual stress generated following the fast cooling from the forging temperature. The mechanical loading was then commenced and continued until either the sample failed or was deemed to have slipped. These measurements were controlled by the LDVT to ensure that the level of localised deformation to be measured by the DIC was in excess of 2% as a minimum.

All tests were carried out at a constant crosshead speed of 4×10^{-3} mm/s and a starting engineering strain rate of 2×10^{-3}/s. The effective gauge length was assumed to be 2mm for all geometries. The size of the effective gauge lengths is central to this study and before the tests were performed it was acknowledged that they may differ to this original assumption of 2mm in size. An accurate determination would be made by use of the in-situ DIC results obtained later. Therefore the decision was taken to keep the crosshead speed constant for all tests, acknowledging that if the effective gauge lengths were greater or smaller than the assumed 2mm, this would mean differing engineering strain rates for each sample.

A typical displacement and temperature versus time plot is shown in Fig. 6 outlining the test procedure.

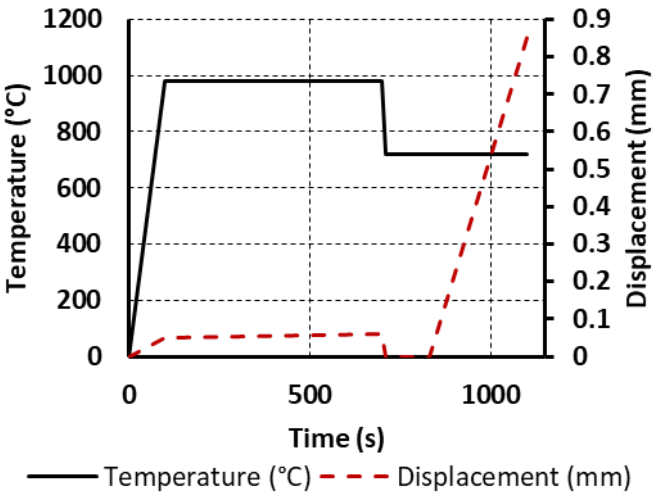

Fig. 6 Typical plot of nominal temperature and displacement profiles against time, applied during a test.

2.2.3 Analysis of temperature distribution by thermal imaging

For the short gauge length and rectangular geometries (Fig. 2), in addition to the temperature measurement using R-type thermo-couples, an arc-thermal imaging camera manufactured by Ametek Land Instruments was also used to measure the temperature distribution over the gauge lengths. The camera had a spectral response of 8 to 14 μm and a field of view of 22°. It had a focus range of 0.3 m to infinity, a maximum recording frequency rate of 30 Hz, and a thermal image resolution of 384 × 288 pixel^2. The camera has an accuracy of ± 2 % or ± 2 °C (whichever was greater) of reading for a blackbody target (i.e., emissivity value of 1).

2.2.4 Determination of mechanical properties at different temperatures using the optimised sample geometry

Following the selection of an optimised sample geometry, additional tests were carried out on the short gauge length sample at various aging temperatures to further ascertain this geometry's suitability in the testing of nickel-based superalloy's by the ETMT system. Similarly, to the test procedure implemented for samples of different geometries, for these tests the samples were initially heated to 980°C at 10 °C/s heating rate and maintained at this temperature for 10 minutes for the annihilation of residual stress and dissolution of existing γ' and γ'' precipitates. The samples were then cooled down to the target aging temperature at a rate of 50° C/s (see Fig. 6). Four tensile tests were carried out at different final aging temperatures including 620˚C, 670˚C, 720˚C and 770˚C. The Young's modulus was calculated for each test via the strain output from the DIC system and the stress calculated from the ETMT system's load cell. The equipment and set-up used were the same as those used for the geometry evaluation tests. Meanwhile, for the evaluation of the surface displacement with DIC system, the strain

maps were obtained using 41 × 41 pixel^2 subset size with a step size of 20. In these tests one pixel was equivalent to 3.65 µm and the image capture rate remained at 10 Hz. Information was only gathered up until the 0.2% yield point as the purpose of these tests was to determine the Young's modulus at the precipitation hardening temperatures, and compare them to the existing data, particularly those measured by conventional tensile test rigs where considerable time (~ 20-30 min) is needed for the sample to reach and stabilise at the target temperature [3].

3 Results

3.1 Effect of sample geometry

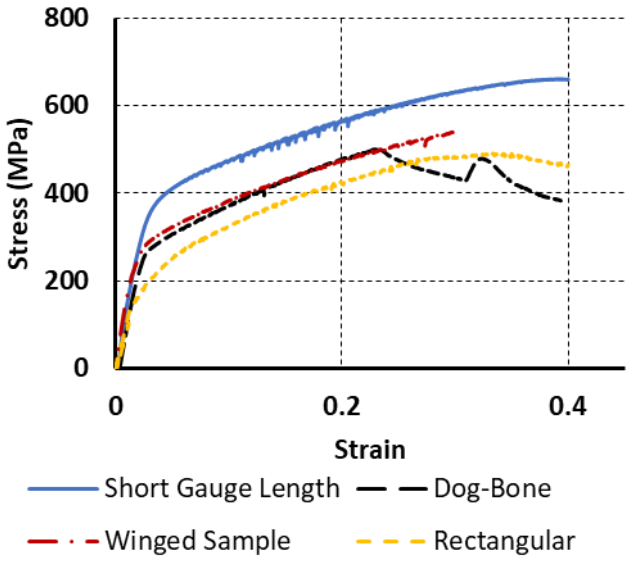

Fig. 7 Plots of stress-strain curves measured by the LVDT interfaced to the ETMT for all sample geometries.

Fig. 7 shows the stress-strain curves plotted using the data recorded by the LVDT and load cell of the ETMT. Firstly, it is important to note that both the dog-bone sample and the rectangular sample showed signs of slip as the tests progressed at 23% and 36% of strain respectively, but the data is still suitable for the majority of the test for comparison with other samples. Secondly, there is a high degree of variation in the stress-strain curves. A reasonable conclusion would be that the only variable in these tests was the sample geometry thus demonstrating the significant impact that this has on the resultant curves. Without the use of DIC, that would have been the conclusion drawn. The reason for this variation was further investigated by use of DIC to plot strain maps to better understand the strain distribution in the ε_{yy} direction.

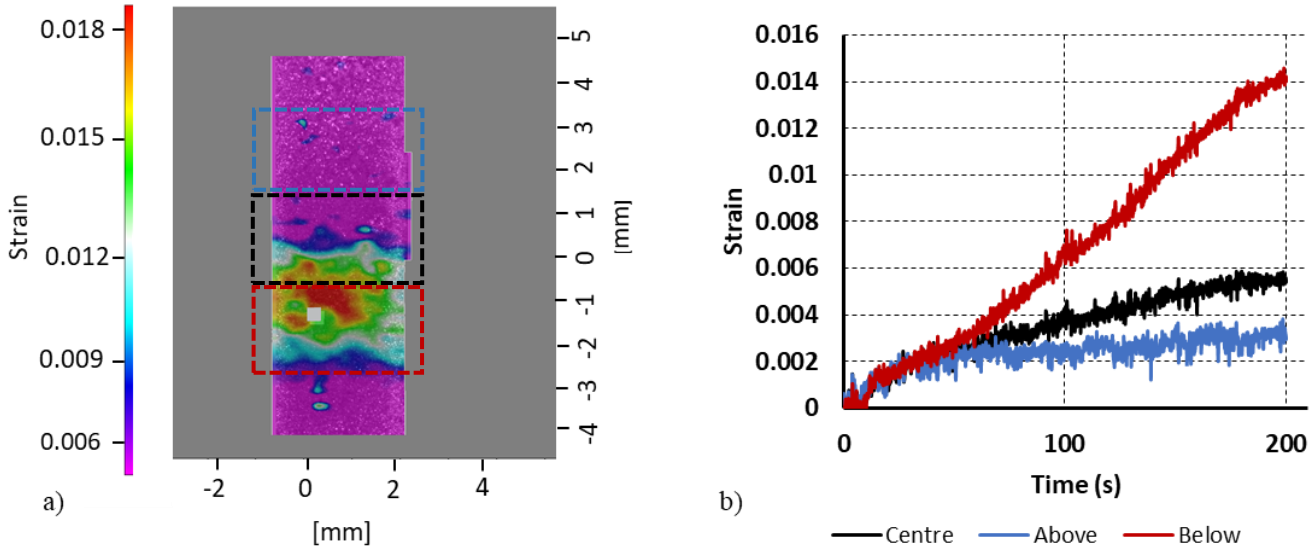

Fig. 8 a) Strain map obtained in the ε_{yy} direction by DIC for the rectangular geometry at 40% strain read-out on the ETMT (i.e., measured by the LVDT) after 200 seconds, and b) plots of strain evolution measured in the ε_{yy} direction by DIC as a function of time for the rectangular geometry over three different areas with a 2mm gauge length each at the middle, above the middle and below the middle section of the sample. Note that the maximum temperature was reached in the centre of the sample.

Fig. 8, Fig. 9, Fig. 10, and Fig. 11 show the strain distribution maps for each of the 4 different sample geometries. In each case, a target of 40% strain of the original 2 mm effective gauge length (i.e., 0.8mm grip-to-grip separation) was applied via the ETMT system. Only the data up to 155 seconds is presented for the winged geometry, after which, significant amounts of slip began to take place which impacted the results. Critically, these strain localisations did not take place in the centre of the sample for most geometries, where the temperature was maximum, as demonstrated in the strain maps. For a clearer demonstration, the mid-section of each sample was divided into three areas with 2 mm gauge length each with no overlap, and the strain evolution as a function of time was evaluated from the DIC data to explore the magnitude of strain localisation. This was to show that the majority of the deformation occurred out with the region where the temperature was the highest.

The strain distribution measured for the rectangular geometry (Fig. 8a) shows the strain localisation 1 mm below the centre point. Fig. 8b shows that despite a small majority of the strain still coming from the centre of the sample, a significant portion of the deformation takes place away from the midsection of the sample, in particular in the 2 mm section immediately below the middle 2 mm mid-section of the sample.

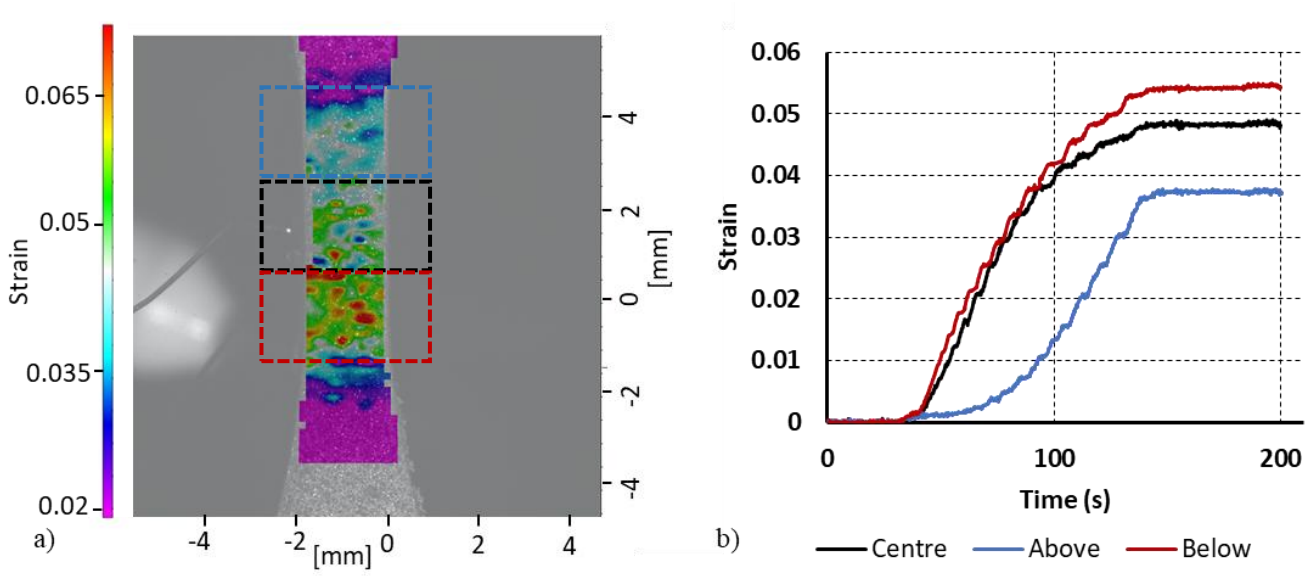

Fig. 9 a) Strain map obtained in the ε_{yy} direction by DIC for the dog-bone geometry at 40% strain read-out on the ETMT (i.e., measured by the LVDT) after 200 seconds, and b) plots of strain evolution measured in the ε_{yy} direction by DIC as a function of time for the dog-bone geometry over three different areas with a 2mm gauge length each at the middle, above the middle and below the middle section of the sample. Note that the maximum temperature was reached in the centre of the sample.

The strain distribution map for the dog-bone geometry shown in Fig. 9a reveals that a significant strain localisation had taken place within the 5 mm gauge length. However, closer inspection shows that the strain concentration was 2.5 mm below the centre of the gauge length. Fig. 9b confirms that the majority of the measured deformation did not occur at the middle of the sample, but rather at the area with 2 mm gauge immediately below the mid-section. Fig. 9b also shows serration in the strain vs time plots which is believed to be quantisation from the virtual strian gauge, this could be due to the size of the virtual strain gauge.

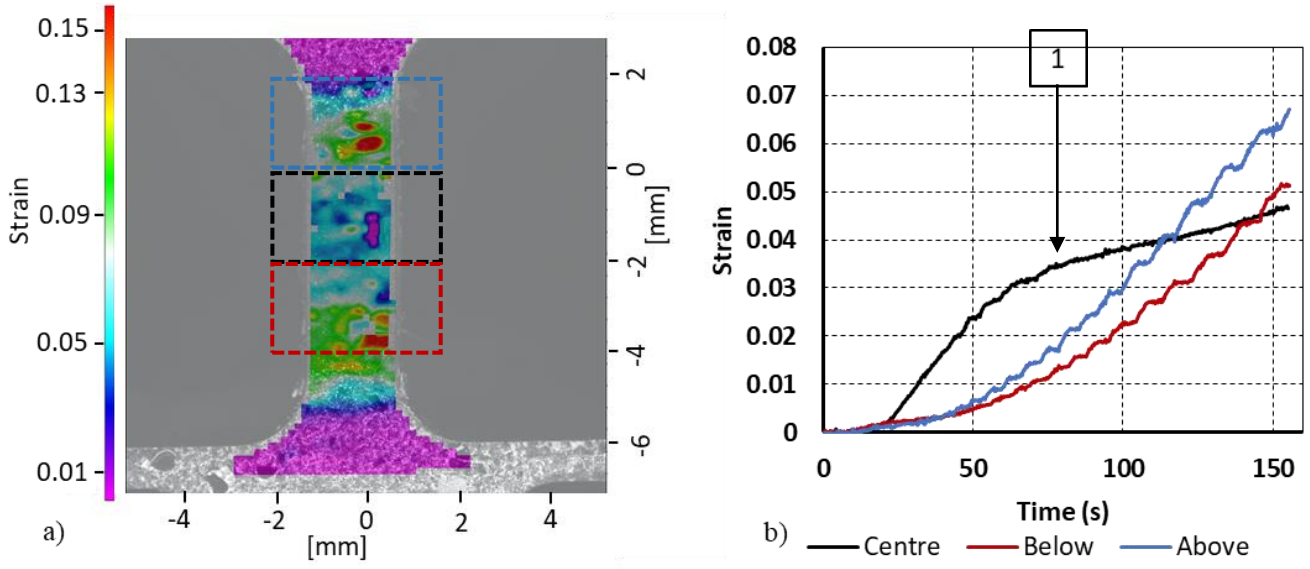

Fig. 10 a) Strain map obtained in the ε_{yy} direction by DIC for the winged geometry at 30% strain read-out on the ETMT (i.e., measured by the LVDT) after 155 seconds, and b) plots of strain evolution measured in the ε_{yy} direction by DIC as a function of time for the winged geometry over three different areas with a 2mm gauge length each at the middle, above the middle and below the middle section of the sample. Note that the maximum temperature was reached in the centre of the sample.

As for the winged geometry, the strain localisation has drifted away from the mid-gauge area to regions between 2 - 2.5 mm above and below the centre, as can be seen in Fig. 10a. After 60 seconds the rate of strain in the mid-section can be seen to drop as the sample hardens in that area (marker 1), and then continues to deform at a lower rate compared to the 2 mm areas immediately above and below. Fig. 10b shows serration in the strain vs time plots suggesting that this sample is showing quantisation because of the use of a virtual strain gauge.

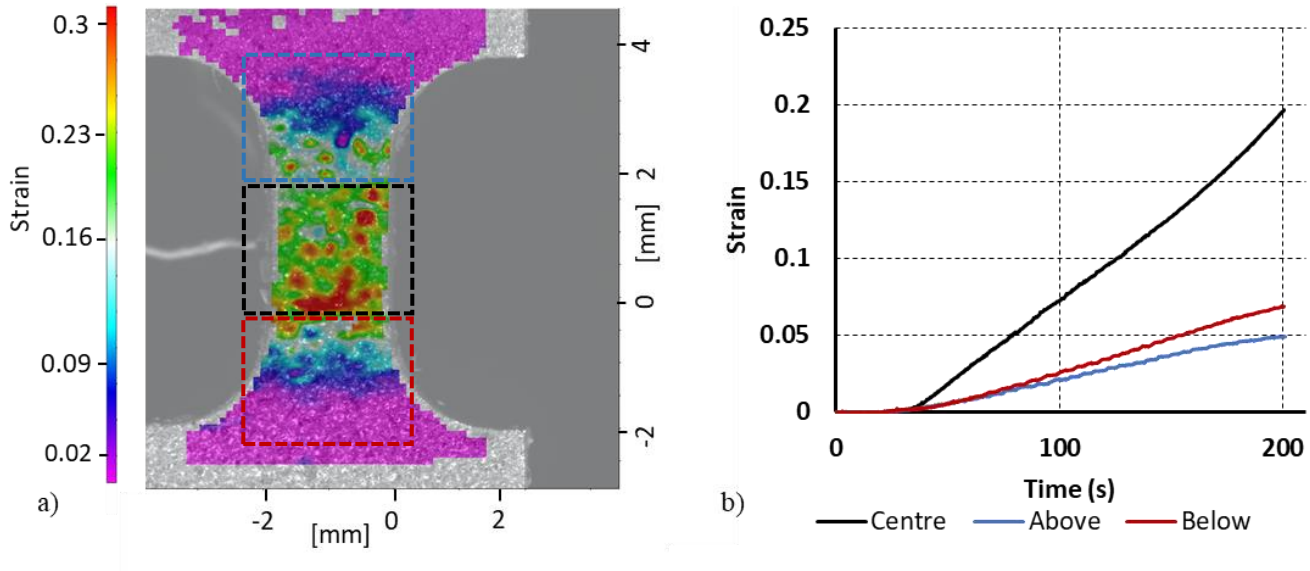

Fig. 11 a) Strain map obtained in the ε_{yy} direction by DIC for the short gauge length geometry at 40% strain read-out on the ETMT (i.e., measured by the LVDT) after 200 seconds, and b) plots of strain evolution measured in the ε_{yy} direction by DIC as a function of time for the short gauge length geometry over three different areas with a 2mm gauge length each at the middle, above the middle and below the middle section of the sample. Note that the maximum temperature was reached in the centre of the sample.

Meanwhile, for the short gauge length geometry, the strain concentration occurred nicely in the central 2 mm gauge length area of the sample satisfying the first condition of no strain drift. For this sample, it appeared (Fig. 11a) that the strain concentration encroaches out-with the 2mm gauge length where the cross sectional area increases due to the fillets, and as Fig. 11b shows, the strain out-with the central 2mm section of the sample is not negligible. This means the second condition of having the gauge length and effective gauge length as the same value is not entirely satisfied, however, this geometry does show a clear majority of strain at the centre. The impact that the strain encroaching into the fillet section has on the strain calculated from the LVDT sensor is analysed more in the discussion section). These measurements and observations suggest that the only sample geometry which satisfies the necessary criteria for appropriate deformation (i.e., localised at the centre-point of the sample),

where the target temperature is reached, is the optimised geometry with short gauge length developed in this study. The short gauge length sample partially meets the second criteria of having the gauge length and the effective gauge length as the same size.

3.2 Temperature distribution

Fig. 12 and Fig. 13 show the temperature distributions measured by a thermal camera for the rectangular and short gauge length samples. The temperature at a position 1 mm above the centre line and 1 mm below the centre line was measured for both samples and gives an indication of the temperature stability across the 2 mm total gauge length. In the case of the rectangular sample, the largest temperature drop was 1.89˚C over the 2 mm gauge length, and for the short gauge length sample, the largest temperature drop was 1.97˚C. This represents a 0.263% and 0.274% difference from the edge of the 2 mm gauge length to the centre for the rectangular and short gauge length samples, respectively.

The NPL's Good practice guide indicates that for a rectangular geometry, the temperature difference across a 2 - 4 mm gauge length is ± 3 ˚C at a temperature of 1250 ˚C, and less than ± 3 ˚C at lower temperatures [6]. The results of these tests carried out using a thermal camera are in good agreement with those from the NPL's Good practice guide. It can therefore reasonably be said that the short gauge length sample likely satisfies the necessary criteria of the temperature remaining as consistent across a 2 mm gauge length with a difference of < 0.28 % at 720˚C.

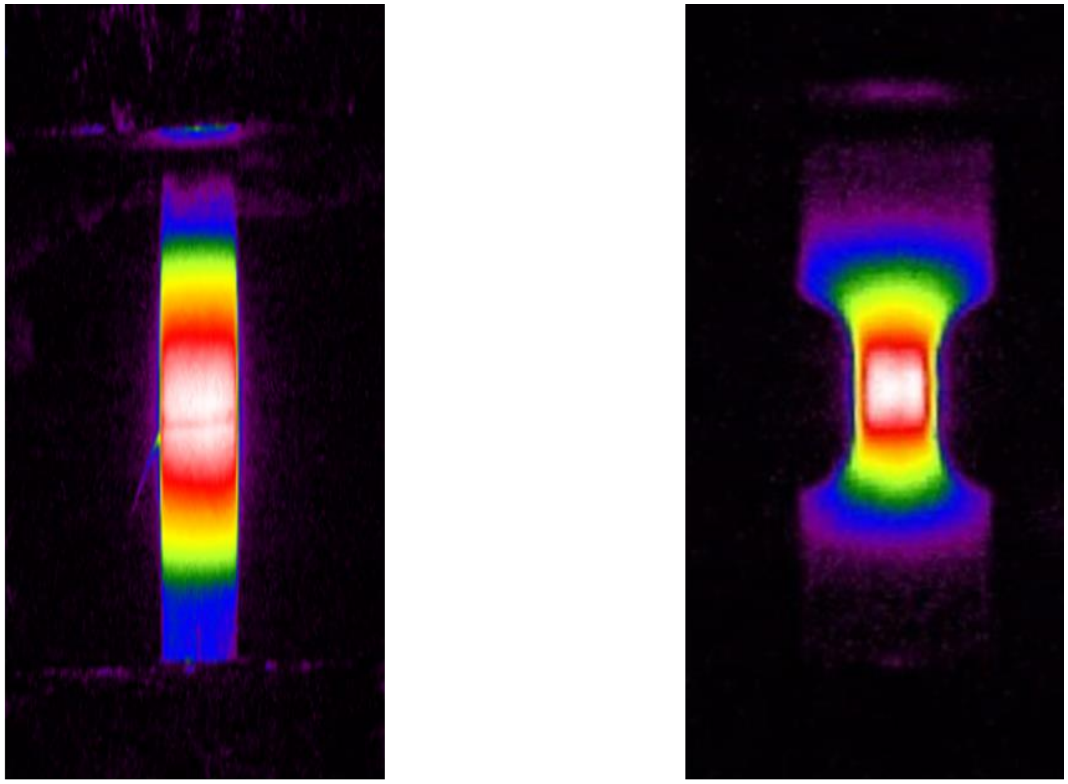

Fig. 12 Temperature distribution maps measured by a thermal camera at 720 °C after a 2-minute dwell across the sample length for (a) a rectangular sample, and (b) a short gauge length sample.

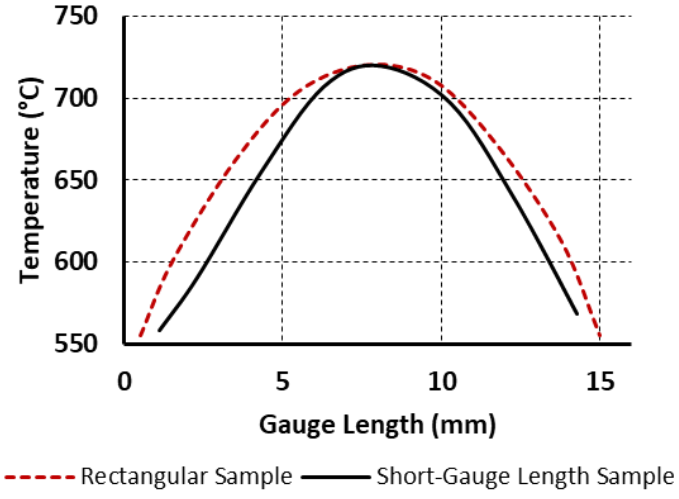

Fig. 13 Temperature distribution plot measured by a thermal camera at 720 °C after a 2-minute dwell across the gauge length of the rectangular sample and the short gauge length sample.

3.3 Temperature dependant mechanical properties

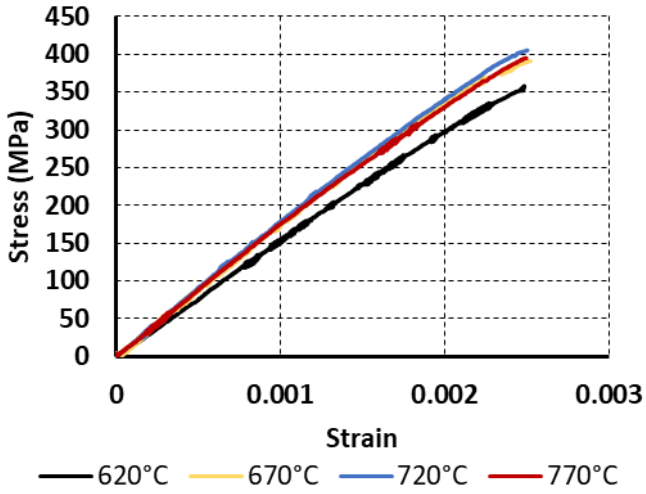

Fig. 14 Plot of stress-strain curves evaluated from the data measured by LVDT on the short gauge length sample for the temperature dependant mechanical properties tests carried out at different temperatures. All tests were done within the elastic limit.

It can be seen Fig. 14 that the results produced from the LVDT sensor of the ETMT are fairly consistent with one another for temperatures between 670°C-770°C. The curve produced for the test carried out at 620°C, shows a less severe slope in the elastic portion of the test meaning that the Young's modulus is noticeably less than for the other tests (see Table 3). It has been shown for this material and at these temperatures that as the aging temperature decreases, the Young's modulus increases [3, 18]. The Young's modulus values calculated from the LVDT sensor of the ETMT do not exhibit this trend as Table 3 shows. The results of the tests carried out at 620˚C and 770˚C give values which are much smaller and much larger respectively when compared with similar tests in literature and shown in Table 3.

Table 3 also shows the measured Young's modulus values at 5 different temperatures on the optimised short gauge length sample geometry calculated by DIC. At all temperatures, the determined Young's modulus values calculated using the DIC are smaller than those from the two other comparable reports. The difference between the Young's modulus at room temperature is relatively small and could be due to differences in the thermal or mechanical processing histories of the materials, or in the chemical compositions. Meanwhile for the tests carried out at the aging temperature range there is a general trend of decreasing Young's modulus as temperature increases for the data calculated using DIC, matching the other two studies. However, at lower aging temperatures the data measured by the DIC were significantly lower than those reported in literature. This is due to the fact that the data reported in literature, including a previous study by the authors [10], were all obtained using conventional testing

rigs equipped with furnaces whereby a significant time (~ 20 – 30 min) was required to reach the target temperature, which is long enough for the precipitation of considerable amount of γ″ [11], leading to a material with higher stiffness. Whereas for the tests conducted with the ETMT, the sample was heated to the target temperature almost instantly (i.e., within a few seconds) with little time for γ″ precipitation to occur, resulting in a material with lower stiffness. Meanwhile, by increasing the temperature towards the ideal temperature for γ″ precipitation (i.e., 720 °C) the difference in the measured Young's modulus by ETMT with those reported in literature reduces. This can be due to the higher kinetics of γ″ precipitation at higher temperatures, meaning that sufficient volume of strengthening precipitate could become present in the material, despite being heated quickly by the ETMT. Note that the material used for these analyses were all solution annealed prior to the test.

Overall there is good agreement in the values emphasising that the short gauge length sample satisfies both the thermal and mechanical criteria needed for a successful mechanical properties (e.g., Young's modulus) determination at elevated temperatures where heavy γ″ precipitation is likely to occur for IN718.

Table 3 Summary of the mechanical properties, including Young's Modulus and yield strength, measured by the ETMT for IN718 nickel-based superalloy in comparison to the data in literature.

Temperature (˚C)	*Young's Modulus calculated from the ETMT LVDT (GPa)*	*Young's Modulus calculated from the ETMT and DIC tests (GPa)*	*Young's Modulus calculated from Rahimi et al.*[3] *(GPa)*	*ASM Specialty Handbook values* [18] *(GPa)*
20	176	183	193	200
620	149	158	184	169
670	166	150	175	164
720	171	155	167	160
770	166	142	143	155

4 Discussion

The material investigated in this study, IN718, is a precipitation hardenable nickel-iron based superalloy containing considerable fractions of Nb and Mo, and small fractions of Ti and Al (see Table 1). This grade of superalloy achieves its superior mechanical strength for high temperature applications from precipitation phases,

predominantly made of Ni_3Nb, with varying fractions of Ti and Al substituting for Nb in form of Ni_3(Al, Ti) [11, 19, 20]. δ-phase, is the most stable form of Ni_3Nb precipitates (≈700°C - 1000°C) that usually nucleates intergranularly (i.e., at grain boundaries), with a possibility of intragranular nucleation (i.e., within grains) in a presence of γ″ precipitate. γ″ is the main strengthening phase in IN718 with thermodynamic stability over the 620°C-900°C temperature range, which has the same chemical stoichiometry (i.e., Ni_3Nb) as that of the δ-phase. Additionally, the existence of a small fraction of γ′ in the microstructure with Ni_3(Al, Ti) form and stability comparable with that of γ″, provides extra strength to the alloy [3, 11, 19–24].

The test plan implemented in this study, included a 10 min annealing at 980°C, followed by cooling to the aging temperature at 50 °C/s rate, and then mechanical testing at this temperature after a 2 min dwell time. The initial annealing temperature leads to the dissolution of all γ′ and γ″ precipitates, and also a minor dissolution of the δ-phase (i.e. less than 10% dissolved), over the majority of the gauge length, since 980°C is approaching the upper limit stability of δ-phase [3, 11]. Due to the parabolic distribution of temperature in the middle section of the sample, the dissolution rate of δ-phase over the gauge length may differ. However, considering the < 2°C difference in the temperature between the extreme ends of the gauge length and the centre of the sample (see Fig. 12 and Fig. 13), the local temperatures are still well beyond γ′ and γ″ stability, and hence these precipitates are all dissolved throughout. When the sample is cooled to the aging temperature range, which is an ideal temperature for γ″ precipitation [11], an onset of precipitation starts to occur at the centre of the gauge length, with reduced precipitation kinetics towards either ends due to the < 2°C difference, caused by parabolic distribution of temperature. This heterogeneity in the precipitation kinetic results in γ″ with different size and distribution throughout the gauge length, which has implications on the mechanical properties.

This is manifested clearly in the flat rectangular geometry proposed by NPL's good practice guide [6] for testing with ETMT, after mechanical testing at 720 °C (see Fig. 8). As can be seen from the strain map in Fig. 8a, localised deformation occurs in a zone which is slightly below the central part of the specimen where the temperature is highest for the rectangular geometry. Fig. 8b shows that the information recorded during the test is only just dominated by the deformation behaviour of the central region, and that the regions out with the area of interest with a known temperature (i.e., where the thermo-couple was installed) show significant levels of strain.

In an attempt to address this problem, a dog-bone geometry (see Fig. 2b) recommended by NPL's good practice guide, which was also used in a previous study [12], was slightly modified and selected as an alternative geometry. As can be seen in Fig. 9a, strain localisation was still observed to consistently occur in a region below the central zone of the sample. Similarly, this indicates that the hardening effect caused by γ″ precipitation was strong enough

to shift the strain localisation away from the middle of the sample where the temperature was the highest and the cross-sectional area was least.

To resolve this problem, the winged geometry was adapted from literature [13]. This geometry was originally designed for testing on a Gleeble 3800, an apparatus that works based on similar principals as those of the ETMT, i.e., both systems use electrical resistivity to heat the samples to the target temperature. However, unlike the ETMT, the sample used for testing with the Gleeble was not miniaturised. Nevertheless, the problem arising from the parabolic temperature distribution across the gauge length was shared by both systems. It was shown in reference [13] that by manufacturing samples with wings extending out from both sides of the sample, above and below the gauge length area (Fig. 2c), and then connecting each side from top to bottom with copper wires, it is possible to make the temperature distribution at the gauge length more homogeneous. This is to create a parallel circuit which would heat the sample and extend the hot zone out from the gauge length. It was thought that a similar design might be deployed for testing with the ETMT using a smaller sample. The geometry manufactured (Fig. 2c) was a refinement of the flat specimen recommended by NPL's good practice guide, with additional wings.

Based on the results of a previous study [13], the winged sample was expected to have a uniform temperature distribution across the gauge length which would in turn lead to a uniform distribution of precipitation and hence deformation. However, Fig. 10a shows that the strain was not evenly distributed throughout the gauge length where a clear shift in strain was observed away from the centre towards the top and the bottom. Therefore, the winged sample, despite its success in testing using the Gleeble 3800 [13], was observed to be unsuitable for testing IN718 at 720°C, using the ETMT. The combination of a miniaturised sample and having a lower current output from the ETMT, which means a sharper parabolic temperature distribution across the gauge length, was likely the cause of this problem.

In all the rectangular, dog-bone and winged sample geometries, deformation occurred out-with the area of interest (i.e., centre of the gauge length) where the temperature was measured to be highest. It was thought that this was predominantly because of the gauge length of these geometries being too long, i.e., 16 mm, 5 mm and 6 mm for the rectangular, dog-bone and winged samples, respectively. Therefore, it was decided to reduce the gauge length to 2 mm in the short gauge length geometry to force the deformation into the centre of the sample. As such, the radii of the fillets for the standard dog-bone sample was 20 mm to avoid any stress localisation that leads to fracture in this area. This was possible when the fillets are too sharp and likely to happen when the material is brittle. However, a radius of 1.5 mm was considered for the optimised geometry. As can be seen in Fig. 11a, the

strain map obtained for the short-gauge length sample with sharp fillets shows deformation centred in the middle of the sample, indicating that it successfully satisfied the first criteria. The third criteria, having a temperature distribution across the gauge length of less than 1% can be seen to have been satisfied as shown in Fig. 12 and Fig. 13. The second criteria of having the effective gauge length equal to that of the actual gauge length is only partially satisfied. The majority of deformation does indeed come from the middle of the sample, far more so than in the case of any other geometry tested, however, there is still a small but significant proportion which does not and comes from areas just outside the central 2mm region. This still means that the sharper fillets combined with the reduced gauge length enabled successful tests of IN718 nickel-based superalloy at the aging temperature range (i.e., 620 °C - 720 °C) to take place, however care must be taken when interpreting strain results from the LVDT sensor.

The Young's modulus is a difficult quantity to measure using DIC due to the small level of displacements to be measured, which can often be smaller than the noise of the DIC [25]. It is however an excellent quantity to measure for the sake of comparison with other reports in literature [3, 18, 26]. As such this was selected as the final qualifying criteria in a bid to find a sample geometry suitable for the determination of thermo-mechanical properties in superalloys. The work carried out by Rahimi et al.[3] was used for comparative purposes, as was the results published in ASM Specialty Handbook [18]. To extract data for the temperatures examined in this study, a linear interpolation was applied to the results from the ASM Specialty Handbook as the exact temperatures did not match up with the test temperatures carried out in these tests.

Finally, an approach has been suggested to equate the strain measured using the DIC system over the 2 mm gauge length of the short gauge length sample, with the strain measured by the LVDT. This was done by correcting the strain measured by the LVDT to the strain measured using the DIC using a generalised reduced gradient solver built into Microsoft excel. The average absolute relative error (AARE) seen in Equation 2, where E_i is the experimental stress values, P_i is the predicted stress values, and N is the number of data points, was used as an objective function and the strain measured using the LVDT was corrected to two different equations and then compared. The first equation was the standard equation of a straight line ($y=mx+c$) and the second equation was the power law ($y=mx^b$). The only constraint applied was for the value of c in the equation of a straight line to equal zero as would have to be the case.

Equation 2

$$AARE\ (\%) = \frac{1}{N}\sum_{i=1}^{N}\left|\frac{E_i - P_i}{E_i}\right| x100$$

Fig. 15a and b shows the plots of strain versus time measured by both the DIC system and the LVDT for both equations. The values for m and b in the power law were 0.740 and 1.289 respectively. The value of m for the equation of a straight line was 0.460. The AARE for the power law equation was 15.15% and the AARE for the equation of a straight line was 28.43% meaning the power law is a better fit at correcting the strain measured from the LVDT sensor of the ETMT to the data from the DIC. This can be seen in Fig. 15a and b where the power law shows a much closer fit than the straight line. Polynomial equations were not selected for comparison as the power law showed good accuracy and was simpler than a polynomial equation for prediction. The reason for the divergence of the uncorrected LVDT strain from the DIC strain, especially at the beginning of a test, is because the LVDT sensor is attached to the grips of the ETMT machine and therefore not sensitive enough to detect the impact of machine compliance and/or that of sample straightening during testing in cases where they haven't been aligned perfectly. The LVDT sensor reads displacement along the sample, even if the sample is yet to fully settle into the grips and align with the direction of tension. DIC is more astute at detecting this phenomenon which is thought to be the reason behind the early divergence in the curves. Thereafter, the difference in strain continues to grow between the uncorrected LVDT strain value and the DIC measured strain. Fig. 11 shows that the majority of the strain comes from the 2mm gauge length in the middle of the sample, but there was still some strain measured out with this gauge length. The strain out with this gauge length is thought to be the reason behind the difference in the uncorrected strain measured from the LVDT and the strain measured using the DIC. Therefore it can be seen that the correction applied is predominantly to address the strain out-with the 2mm gauge length in the centre of the sample. Constitutive models have been used to predict the flow stress at elevated temperatures [27–31], however, it is well known that a constitutive model is heavily dependent on the material characteristics (i.e., microstructure), the strain rate and the temperature which the tests were carried out at. Therefore it is assumed that further work would need to be carried out to determine the robustness of Equation 3, and to see if it is representative of all precipitation hardened materials, and for what temperature and strain rate regimes.

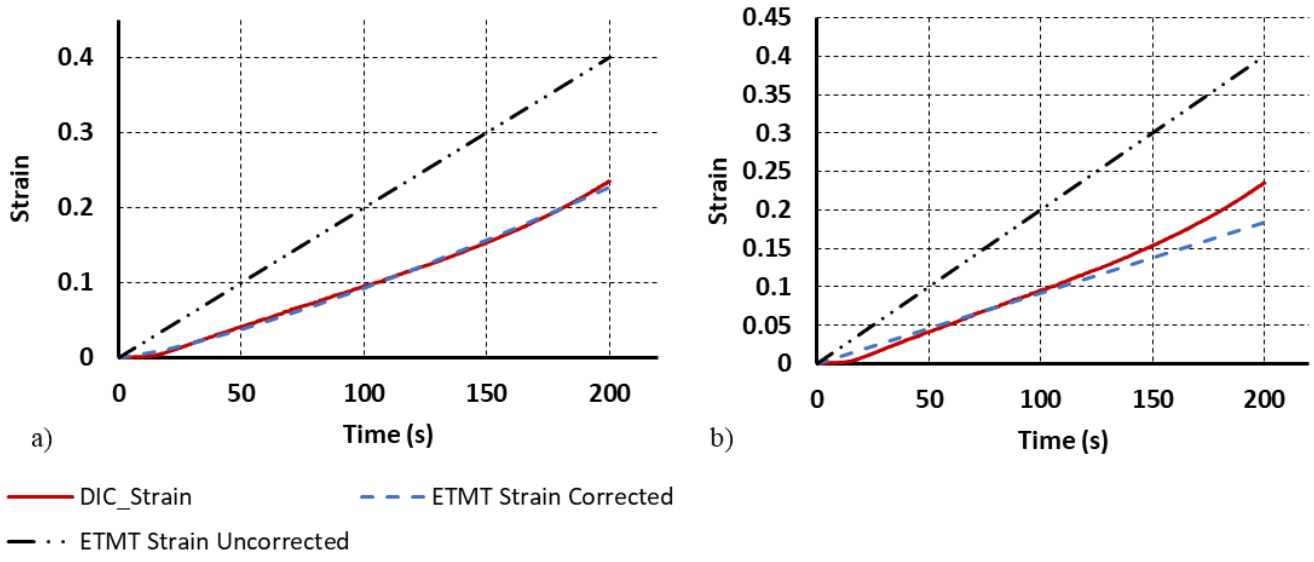

Fig. 15 a) Plots of strain vs time at 720˚C for the uncorrected LVDT strain, the strain measured by DIC and a) strain data collected from the LVDT sensor of the ETMT and corrected using a power law equation and b) strain data collected from the LVDT sensor of the ETMT and corrected using the equation of a straight line.

Equation 3

$$\varepsilon_{ETMTcorrected} = 0.74 * \varepsilon_{ETMTuncorrected}1.289$$

Where $\varepsilon_{ETMTcorrected}$ is the strain measured from the LVDT sensor of the ETMT after correction to the strain measured by the DIC system and $\varepsilon_{ETMTuncorrected}$ is the strain measured directly from the LVDT sensor on the ETMT. This approach enables one to confidently rely on the strain measured by the LVDT without a need for a DIC system. The authors recommend further work to understand the impact which temperature and strain rate have on this equation, as well as its applicability with other precipitation hardened materials. Furthermore, the development of this empirical equation though rooted in practicality, could potentially be better strengthened if it were to be rooted in a physical-based model. This would require additional data at different temperatures and strain rates which were beyond the scope of this work. Although, additional data is needed to verify this approach for other materials as the coefficients can vary, the proposed methodology works for the IN718 nickel-based superalloy at a temperature of 720˚C, for a starting engineering strain rate of 2 ×10-3/s. Nevertheless, the sample geometry is essential in obtaining the correct data for this class of materials (i.e., precipitation hardenable) by the aid of ETMT, and this study has demonstrated the appropriate sample geometry.

5 Conclusion

Four different sample geometries were examined to determine their suitability for thermo-mechanical testing of a precipitation hardenable material, IN718 nickel-based superalloy, using an ETMT system. The following conclusions can be drawn:

- The results of surface displacement and strain mapping by the aid of digital image correlation showed that in all geometries strain localisation occurred away from the centre of the gauge lengths of the samples, where the deformation is expected to be, with the exception of a modified geometry with a short gauge length. This sample showed strain localisation perfectly at the centre of the sample.
- The short gauge length sample showed 0.274% difference in temperature between the centre of the gauge length and its 2 mm outer edge at a temperature of 720°C. In comparison, this value was 0.263% for the standard rectangular sample over a matching 2 mm gauge length and at the same temperature.
- The short gauge length sample is suitable for determining arguably the most difficult of mechanical properties, the Young's modulus, for the precipitation hardenable material IN718 at room temperature, as well as at aging temperatures in the region of 620˚C to 770˚C where significant γ' and γ'' precipitation takes place making the material stronger, by making use of digital image correlation.
- These results suggest that the modified geometry designed, tested and verified in this study is in fact suitable for mechanical testing of precipitation hardenable materials, such as nickel-based superalloys, at elevated temperatures.
- A methodology is proposed to facilitate the use of the short gauge length sample in accurately determining the strain from the ETMT's LVDT sensor for IN718 nickel-based superalloy.

6 Acknowledgements

The experimental works were carried out at the Advanced Forming Research Centre (AFRC), University of Strathclyde, which receives partial financial support from the UK's High Value Manufacturing CATAPULT.

7 Conflict of Interest

This work has not been previously published. This work is also part of an ongoing doctoral thesis for the first named author. The authors of this paper have no conflicts of interest to declare.

8 References

1. Devaux A, Picqué B, Gervais MF, et al (2012) AD730 ™ - A New Nickel-Based Superalloy for High Temperature Engine Rotative Parts. In: Superalloys 2012. pp 911–919
2. Devaux A, Georges E, Héritier P (2011) Development of New C&W Superalloys for High Temperature Disk Applications. Adv Mater Res 278:405–410. https://doi.org/10.4028/www.scientific.net/AMR.278.405
3. Rahimi S, King M, Dumont C (2017) Stress relaxation behaviour in IN718 nickel based superalloy during ageing heat treatments. Mater Sci Eng A 708:563–573. https://doi.org/10.1016/j.msea.2017.09.116
4. ASTM E8 (2021) ASTM E8/E8M standard test methods for tension testing of metallic materials
5. ASTM E21 (2020) AST E21 Standard Test Methods for Elevated Temperature Tension Tests of Metallic Materials
6. Roebuck B, Brooks M, Pearce A (2016) Good Practice Guide for Miniature ETMT Tests, 1st ed. National Physical Laboratory, London
7. Roebuck B, Cox DC, Reed RC (2004) An Innovative Device for the Mechanical Testing of Miniature Specimens of Superalloys
8. Roebuck B, Gee MG, Lord JD, McCartney LN (1998) Miniature thermal cycling tests on aluminium alloy metal matrix composites. Mater Sci Technol 14:1001–1008
9. Kardoulaki E., Lin J., Balint D., Farrugia D. (2014) Investigation of the effects of thermal gradients present in Gleeble high-temperature tensile tests on the strain state for free cutting steel. J Strain Anal Eng Des 49:521–532. https://doi.org/10.1177/0309324714531950
10. Konkova T, Rahimi S, Mironov S, Baker TN (2018) Effect of strain level on the evolution of microstructure in a recently developed AD730 nickel based superalloy during hot forging. Mater Charact

139:437–445. https://doi.org/10.1016/j.matchar.2018.03.027

11. Brooks JW, Bridges PJ (1988) Metallurgical Stability of Inconel 718. Superalloys 1988 Symp 33–42. https://doi.org/10.7449/1988/Superalloys_1988_33_42

12. Sulzer S, Alabort E, Németh A, et al (2018) On the Rapid Assessment of Mechanical Behavior of a Prototype Nickel-Based Superalloy using Small-Scale Testing. Metall Mater Trans A Phys Metall Mater Sci 49:4214–4235. https://doi.org/10.1007/s11661-018-4673-5

13. Ganapathy M, Li N, Lin J, et al (2015) Analysis of new Gleeble tensile specimen design for hot. 05013:0–6

14. Ma C, Zeng Z, Zhang H, Rui X (2019) A correction method for heatwave distortion in digital image correlation measurements based on background-oriented schlieren. Appl Sci 9:. https://doi.org/10.3390/app9183851

15. Jones EMC, Reu PL (2018) Distortion of Digital Image Correlation (DIC) Displacements and Strains from Heat Waves. Exp Mech 58:1133–1156. https://doi.org/10.1007/s11340-017-0354-3

16. Valeri G, Koohbor B, Kidane A, Sutton MA (2017) Determining the tensile response of materials at high temperature using DIC and the Virtual Fields Method. Opt Lasers Eng 91:53–61. https://doi.org/10.1016/j.optlaseng.2016.11.004

17. Bigger R, Blaysat B, Boo C, et al (2018) A Good Practices Guide for Digital Image Correlation. Int Digit Image Correl Soc 94

18. Davis JR, Committee ASMIH (2000) Nickel, Cobalt, and Their Alloys. ASM International

19. Barker JF, Ross EW, Radavich JF (1970) Long Time Stability of Inconel 718. J Met 22:31–41. https://doi.org/10.1007/bf03355624

20. Caliari FR, Guimarães NM, Reis DAP, et al (2013) Study of the Secondary Phases in Inconel 718 Aged Superalloy Using Thermodynamics Modeling. Key Eng Mater 553:23–28. https://doi.org/10.4028/www.scientific.net/KEM.553.23

21. Akca E, Gursel A, Gürsel A (2015) A Review on Superalloys and IN718 Nickel-Based INCONEL Superalloy. Period Eng Nat Sci 3:. https://doi.org/10.21533/pen.v3i1.43

22. Lacaze J, Dehmas M, Niang A, Viguier B (2011) TEM study of high-temperature precipitation of delta

phase in inconel 718 alloy. Adv Mater Sci Eng 2011:. https://doi.org/10.1155/2011/940634

23. Azadian S, Wei L-Y, Niklasson F, Warren R (2001) Precipitation in Spray-Formed in 718. pp 617–626

24. Kuo CM, Yang YT, Bor HY, et al (2009) Aging effects on the microstructure and creep behavior of Inconel 718 superalloy. Mater Sci Eng A 510–511:289–294. https://doi.org/10.1016/j.msea.2008.04.097

25. Grant BMB, Stone HJ, Withers PJ, Preuss M (2009) High-temperature strain field measurement using digital image correlation. J Strain Anal Eng Des 44:263–271. https://doi.org/10.1243/03093247JSA478

26. Aba-Perea PE, Pirling T, Withers PJ, et al (2016) Determination of the high temperature elastic properties and diffraction elastic constants of Ni-base superalloys. Mater Des 89:856–863. https://doi.org/10.1016/j.matdes.2015.09.152

27. Souza PM, Sivaswamy G, Bradley L, et al (2022) An innovative constitutive material model for predicting high temperature flow behaviour of inconel 625 alloy. J Mater Sci 57:20794–20814. https://doi.org/10.1007/s10853-022-07906-1

28. Tan G, Li H zhong, Wang Y, et al (2021) Physical-Based Constitutive Modeling of Hot Deformation in a Hot-Extruded Powder Metallurgy Nickel-Based Superalloy. J Mater Eng Perform 30:794–804. https://doi.org/10.1007/s11665-020-05291-x

29. Wu J, Jiang Y, Deng W, Yao G The hot deformation behaviors and constitutive modeling of Hastelloy C276 The hot deformation behaviors and constitutive modeling of Hastelloy C276

30. Souza PM, Beladi H, Singh R, et al (2015) Constitutive analysis of hot deformation behavior of a Ti6Al4V alloy using physical based model. Mater Sci Eng A 648:265–273. https://doi.org/10.1016/j.msea.2015.09.055

31. Bodunrin MO (2020) Flow stress prediction using hyperbolic-sine Arrhenius constants optimised by simple generalised reduced gradient refinement. J Mater Res Technol 9:2376–2386. https://doi.org/10.1016/j.jmrt.2019.12.070